

# Rupture Process of the $M_w$ 5.8 Pawnee, Oklahoma, Earthquake from Sentinel-1 InSAR and Seismological Data

by Raphaël Grandin, Martin Vallée, and Robin Lacassin

## ABSTRACT

Since 2009, Oklahoma has experienced a soar in induced seismicity, a side effect of extensive saltwater injection into subsurface sedimentary rocks. The seismic hazard entailed by these regional-scale injection operations is, however, difficult to assess. The 3 September 2016  $M_w$  5.8 Pawnee earthquake is the largest since the increase of seismic activity. The event was preceded by an  $m_b$  3.2 foreshock two days prior, and changes in injection rates have been reported on wastewater disposal wells located less than 10 km from the epicenter, suggesting that the earthquake may have been induced. Using Sentinel-1 spaceborne interferometric synthetic aperture radar, we unambiguously show that the earthquake produced peak-to-peak line-of-sight displacement of 3 cm at the surface. Kinematic inversion of geodetic and seismological data shows that the main seismic rupture occurred between a depth of 4 and 9 km, over a length of 8 km, with slip reaching at least 40 cm. The causative fault is entirely buried within the Precambrian basement, that is, well beneath the Paleozoic sedimentary pile where injection is taking place. Potentially seismogenic faults in the basement of Oklahoma being poorly known, the risk of  $M_w \geq 6$  events triggered by fluid injection remains an open question.

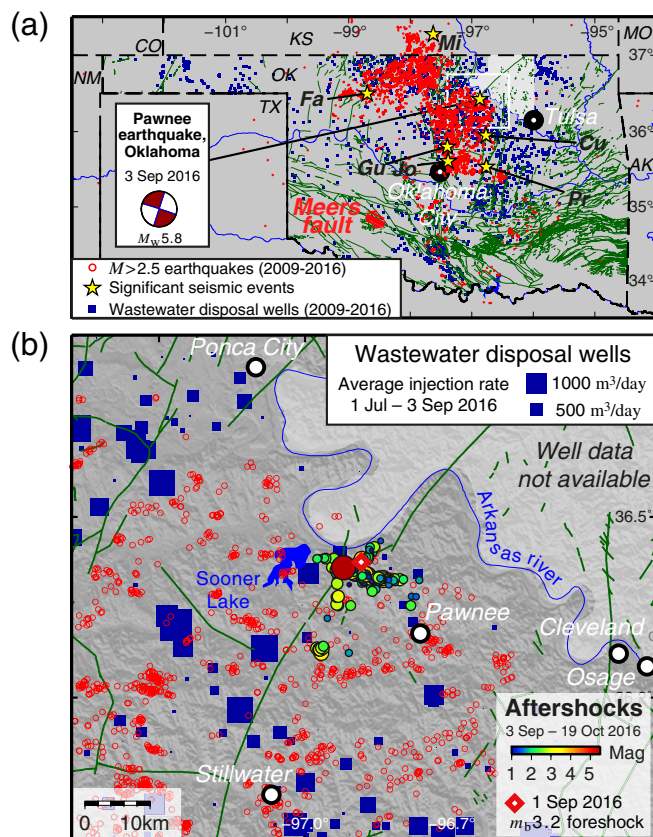
## INTRODUCTION

Central United States, and in particular the state of Oklahoma, has experienced a marked increase in seismicity rate since 2009 (Ellsworth, 2013; Hough and Page, 2015; Frohlich *et al.*, 2016). A body of evidence, the most compelling being the temporal and spatial coincidence (Fig. 1a), strongly suggests that this enhanced seismic activity is primarily induced by the injection of large volumes of wastewater into porous sedimentary formations (Walsh and Zoback, 2015; Weingarten *et al.*, 2015). Injected wastewater consists of variable proportions of coproduced water naturally present in the reservoir and coming out with oil and gas, as well as of flowback of fluids previously injected in the reservoir for enhanced recovery, or fracking (e.g., Rubinstein and Mahani, 2015). As oil and gas exploitation in continental United States has boomed in the last decade, the amount of produced wastewater followed the same trend.

The issue is particularly acute in Oklahoma because wastewater is being injected on a regional scale. The necessity of disposing of enormous volumes of wastewater arises from an exceptionally high volume ratio of produced saltwater:fossil fuel, as large as 7–9 in some parts of Oklahoma, as opposed to 1 or less in other regions (Murray, 2014). Such a high ratio originates from increasing exploitation of unconventional reservoirs by stimulated production techniques (Matson, 2013; Murray, 2015; Rubinstein and Mahani, 2015). The bulk of the coproduced saltwater is mainly injected into the Arbuckle group, which consists of underpressured Ordovician–Cambrian limestones and dolomites (Murray, 2015). These formations are located at the very bottom of the sedimentary pile, just above contact with the crystalline basement.

The dramatic increase in the number of felt earthquakes raised legitimate concern about the possibility of triggering even larger earthquakes. To help answer this pressing issue, studying past and present seismic activities in this previously seismically quiet intraplate region is an obvious need. Most of the well-recorded seismicity in the area lies within the Precambrian basement (Keranen *et al.*, 2013, 2014; McNamara, Benz, *et al.*, 2015; Choy *et al.*, 2016; Yeck, Weingarten, *et al.*, 2016). This observation suggests that faults located at seismogenic depth (5–15 km) could be destabilized by injection operations carried out in the shallow subsurface. Unfortunately, because of the lack of coseismic ground deformation measurements, rupture area of the largest recent earthquakes could not be easily determined. Hence, the actual radius of influence of injection operations, although suspected to be greater than 10 km horizontally and perhaps 5–10 km vertically (Keranen *et al.*, 2013; Choy *et al.*, 2016; Shirzaei *et al.*, 2016; Yeck, Weingarten, *et al.*, 2016), remains subject to uncertainty.

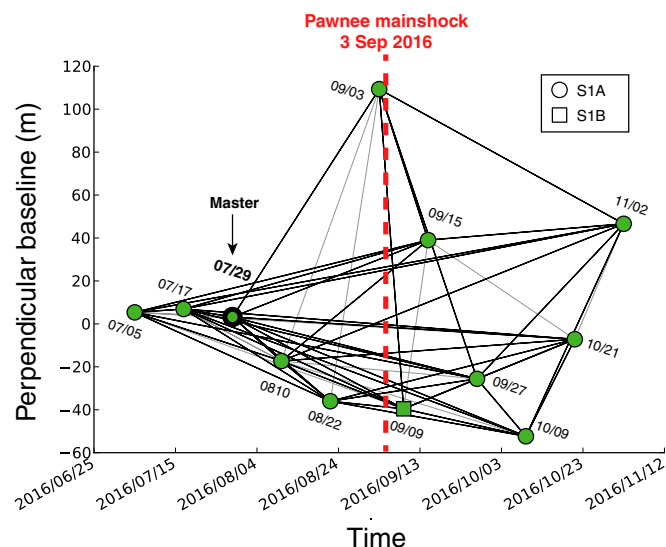
The 3 September 2016  $M_w$  5.8 Pawnee earthquake is the largest reported earthquake in Oklahoma since the recent increase of seismicity. The earthquake induced very strong shaking in the epicentral region (MMI VII), causing damage to some buildings in the epicentral area (see Data and Resources). The aftershock sequence of the Pawnee earthquake was precisely recorded thanks to rapid deployment of a seismic network (Yeck, Hayes, *et al.*, 2016). Aftershock seismicity is concentrated at ~6 km depth, delineating an east-southeast



▲ **Figure 1.** (a) Class II wastewater disposal wells in the 2009–2016 period (squares) and seismicity with  $M > 2.5$  reported by U.S. Geological Survey (USGS) for the same period (circles). Mapped faults are shown in the background (Holland, 2015). Recent clusters of seismicity are indicated by stars. Fa, 2016  $M_W^{\max}$  5.1 Fairview (Yeck, Weingarten, et al., 2016); Mi, 2014  $M_W^{\max}$  4.9 Milan (Choy et al., 2016); Gu, 2014  $M_W^{\max}$  4.0 Guthrie (Benz et al., 2015); Jo, 2009–2014 Jones (Keranen et al., 2014); Cu, 2014  $M_W^{\max}$  4.3 (McNamara, Hayes, et al., 2015) and 2016  $M_W^{\max}$  5.0 Cushing; Pr, 2011  $M_W^{\max}$  5.7 Prague (Keranen et al., 2013). (b) Disposal wells in the area of the 2016 Pawnee earthquake (rectangle in a) are indicated by squares scaled according to the average injection rate in the two months prior to the Pawnee mainshock. Solid circles are aftershocks of the Pawnee earthquake reported by Yeck, Hayes, et al. (2016) scaled according to the magnitude. Diamond indicates the 1 September 2016 foreshock (Yeck, Hayes, et al., 2016). Empty circles represent the USGS seismicity in the 2009–2016 period as in (a). The color version of this figure is available only in the electronic edition.

(ESE)–west-northwest (WNW)–trending vertical fault (Fig. 1b). However, the depth and slip area of the causative fault involved in mainshock remain poorly constrained.

Interferometric synthetic aperture radar (InSAR) has proved to be a powerful tool to characterize seismic and aseismic deformation induced by hydrologic effects of human activity (e.g., Barnhart et al., 2011; González et al., 2012; Yeck, Hayes, et al., 2016). Yet, previous  $M > 5$  earthquakes in Oklahoma could not be studied by InSAR due to lack of sufficient



▲ **Figure 2.** Spatiotemporal relation between acquisitions used in this study. Vertices represent Sentinel-1 acquisitions in a baseline–time diagram, whereas lines connecting the acquisitions correspond to computed interferograms. Thin gray lines indicate interferograms that were discarded due to poor quality. Sentinel-1A acquisitions correspond to circles, whereas the only Sentinel-1B acquisition is indicated by a square. Master image is indicated by a thicker symbol. Mainshock date is marked by vertical dashed line. The color version of this figure is available only in the electronic edition.

observations. As a consequence, the combined effect of decorrelation and atmospheric noise could not be overcome, explaining why these small events have remained, so far, undetectable from space. The new Sentinel-1 system of the European Space Agency (ESA), consisting of two twin satellites launched in April 2014 and April 2016, operating in a novel wide-swath acquisition mode, has recently allowed for significant improvements in terms of detection of small deformation signals (e.g., Geudtner et al., 2014). Because of the relatively strong magnitude of the Pawnee earthquake, the static coseismic surface displacement was deemed sufficient for a measurement using the Sentinel-1 system.

In the following, using this geodetic information together with seismic waves recorded at close and far distances, we analyze the spatiotemporal rupture process of this moderate earthquake. Its relationship with injection operations and implications in terms of seismic hazard are also discussed.

## INSAR PROCESSING METHODS

To isolate the static surface deformation induced by the Pawnee earthquake, we collected data acquired by ESA's Sentinel-1 satellites before and after the earthquake and computed a number of interferograms spanning different time intervals. We selected images from relative orbit 34, which provide the most complete temporal coverage (Fig. 2). They are acquired in ascending pass with an incidence angle of  $41^\circ$  in the epicentral area. An anomaly is indeed detected in the epicentral area for

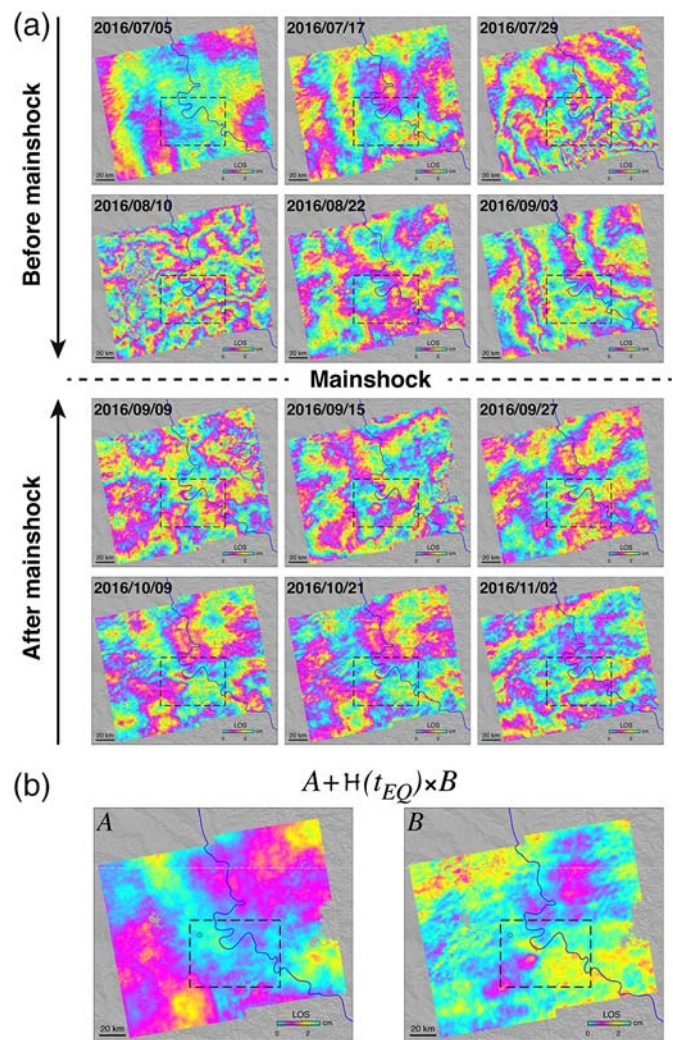


interferograms bracketing the earthquake. However, because of the small magnitude of the displacement (a few centimeters), individual interferograms are dominated by atmospheric turbulence (Yeck, Hayes, *et al.*, 2016). To improve the signal-to-noise ratio (SNR), we compute a time series of the line-of-sight (LoS) signal with a temporal resolution of 12 days. This fine temporal resolution, which is a unique capability of the Sentinel-1 system, makes it possible to isolate the subtle signal associated with the earthquake by averaging out temporally uncorrelated atmospheric disturbances.

Sentinel-1 TOPS data are first preprocessed using the method described in Grandin (2015). The NSBAS software (Doin *et al.*, 2011), which partly relies on ROI\_PAC (Rosen *et al.*, 2004) for individual interferometric calculation, is then used for time-series processing. We use six images acquired prior to the mainshock and six images acquired after. After coregistration onto a single master image (29 July 2016), a total of 55 interferograms are computed (Fig. 2). The choice of the interferograms is based on a minimization of the perpendicular baseline and a minimum redundancy of seven interferograms for any acquisition. Topography is removed using a 10-m resolution digital elevation model from the National Elevation Dataset (Gesch *et al.*, 2002). To improve the SNR, interferograms are then multilooked by a factor 128 in range and 32 in azimuth, leading to a ground posting of  $\sim 500$  m, and an adaptive filter is applied (Goldstein and Werner, 1998). Finally, unwrapping is performed using the branch-cut algorithm (Goldstein *et al.*, 1988).

Using NSBAS software, a time series is computed from the interferograms using a small-baseline approach, which consists in isolating the apparent LoS signal corresponding to each time interval separating two consecutive acquisitions (e.g., Berardino *et al.*, 2002; Schmidt and Bürgmann, 2003). Nine interferograms corrupted by large-scale unwrapping errors are first removed from the analysis. A first iteration is carried out to identify and correct small unwrapping errors, which are detected according to the pixelwise misclosure they provoke in the interferometric network (Cavalié *et al.*, 2007; López-Quiroz *et al.*, 2009). Pixels leading to a residual root mean square (rms) misclosure exceeding 2.5 radian (equivalent to 1.1 cm) are rejected. This cutoff was chosen by trial and error to exclude points evidently corrupted by residual small-scale unwrapping errors.

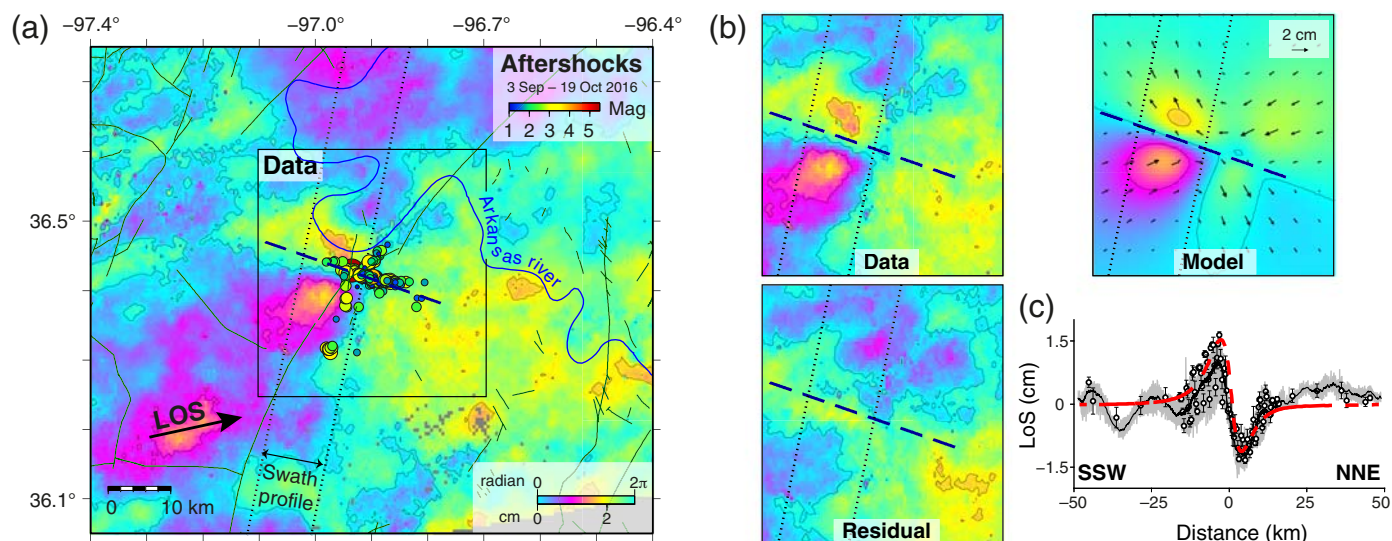
Low-pass temporal filtering is then applied in the time-series inversion to separate any steadily accumulating signal (either due to deformation, e.g., Shirzaei *et al.*, 2016, or seasonally aliased atmospheric phenomena, e.g., Doin *et al.*, 2009) from the erratic contribution of atmospheric turbulence and earthquake signal. According to this test, no steady signal could be detected in the time series, meaning that deformation can be entirely interpreted as coseismic, the remaining contribution to phase variations being temporally uncorrelated atmospheric turbulence. As a consequence, the low-pass filtering step is discarded in the following to avoid aliasing of the coseismic signal. A second iteration is performed by weighting interferograms by the inverse of the rms residual in each time step. In the third iteration, another subset of two interferograms affected by large atmospheric noise, corresponding to the largest overall residual,



▲ **Figure 3.** (a) Line-of-sight (LoS) cumulative interferometric signal as a function of time decomposed on each time interval separating two successive acquisitions. Interferograms are here unwrapped and rewrapped with a color palette cycle of 2.5 cm for the purpose of facilitating interpretation. The dashed rectangle indicates epicentral region of the Pawnee earthquake, whereas the six upper panels represent acquisitions preceding the earthquake, whereas the six lower panels are for acquisitions made after the earthquake. (b) LoS displacement deduced from pixelwise inversion using a model consisting of a constant ( $A$ ) and a step function ( $B$ ) (equation 1). The color version of this figure is available only in the electronic edition.

is discarded. An unfiltered time-series inversion is finally performed using the 44 remaining interferograms (Fig. 3a).

At this stage, the phase changes corresponding to each time interval separating consecutive acquisitions are determined. They include both the atmospheric fluctuations and the coseismic earthquake signal. To isolate the contribution of the Pawnee mainshock, we use a simple forward model consisting of the sum of a constant term  $A$  (corresponding to atmospheric noise in the reference image) and a step function  $H$  with amplitude  $B$  (the earthquake signal), synchronized with the date of the earthquake  $t_{EQ}$ :



**▲ Figure 4.** (a) Ground deformation for the period spanning the Pawnee mainshock derived from Sentinel-1 interferometric synthetic aperture radar. Background shows motion in the LoS of the satellite using a color palette cycle of 2.5 cm. Positive is for motion away from the satellite and negative is for motion toward the satellite. The LoS direction is indicated by the arrow at the bottom left. The dashed line marks the surface projection of the upper edge of the modeled fault. Circles and lines are aftershocks and faults, respectively, as in Figure 1. (b) Enlarged view of the epicentral area (highlighted by rectangle in a) showing observed, modeled, and residual displacement. The model is here computed from the kinematic slip model, deduced from joint inversion of geodetic and seismological data. Arrows indicate predicted horizontal components of surface displacement. (c) Comparison of observed and synthetic LoS displacement along swath profile is indicated by the thin dotted lines in (a) and (b). The thin continuous line is the observed displacement averaged in 0.5 km bins in a 10-km-wide swath profile, with the gray band in the background indicating the data range in the swath profile. Circles show decimated data used as input for the inversion and associated error bars. The thick dashed line is synthetic displacement from finite-source kinematic inversion sampled in the middle of the swath profile. The color version of this figure is available only in the electronic edition.

$$A + H(t_{EQ}) \times B. \quad (1)$$

Misfits between observation and model are interpreted as reflecting atmospheric artifacts. Using the forward model  $\mathbf{d} = \mathbf{G}\mathbf{m}$ , in which  $\mathbf{d}$  is the data column vector,  $\mathbf{m}$  is the column vector of model parameters, and  $\mathbf{G}$  is the design matrix containing ones and zeros, corresponding to the discretization of equation (1), the weighted least-squares problem is solved as

$$\hat{\mathbf{m}} = (\mathbf{G}'\mathbf{W}\mathbf{G})^{-1}\mathbf{G}'\mathbf{W}\mathbf{d}. \quad (2)$$

Weights in  $\mathbf{W}$  are determined by assessing the level of noise in the maps of incremental deformation from each time interval. This is achieved by computing empirical semivariograms clipped to a maximum distance  $x$  of 75 km (after masking out the deformation area), and fitted with an exponential model with expression  $S^2 * [1 - \exp(-x/r)] + n$ . We use the asymptotic semivariance in the exponential model  $S_i^2$  to quantify the uncertainty associated with each time step interferogram  $i$ . These values are then used to fill a weight matrix  $\mathbf{W} = \text{diag}(1/S_i^2)$  used to solve the pixelwise weighted least-squares problem.

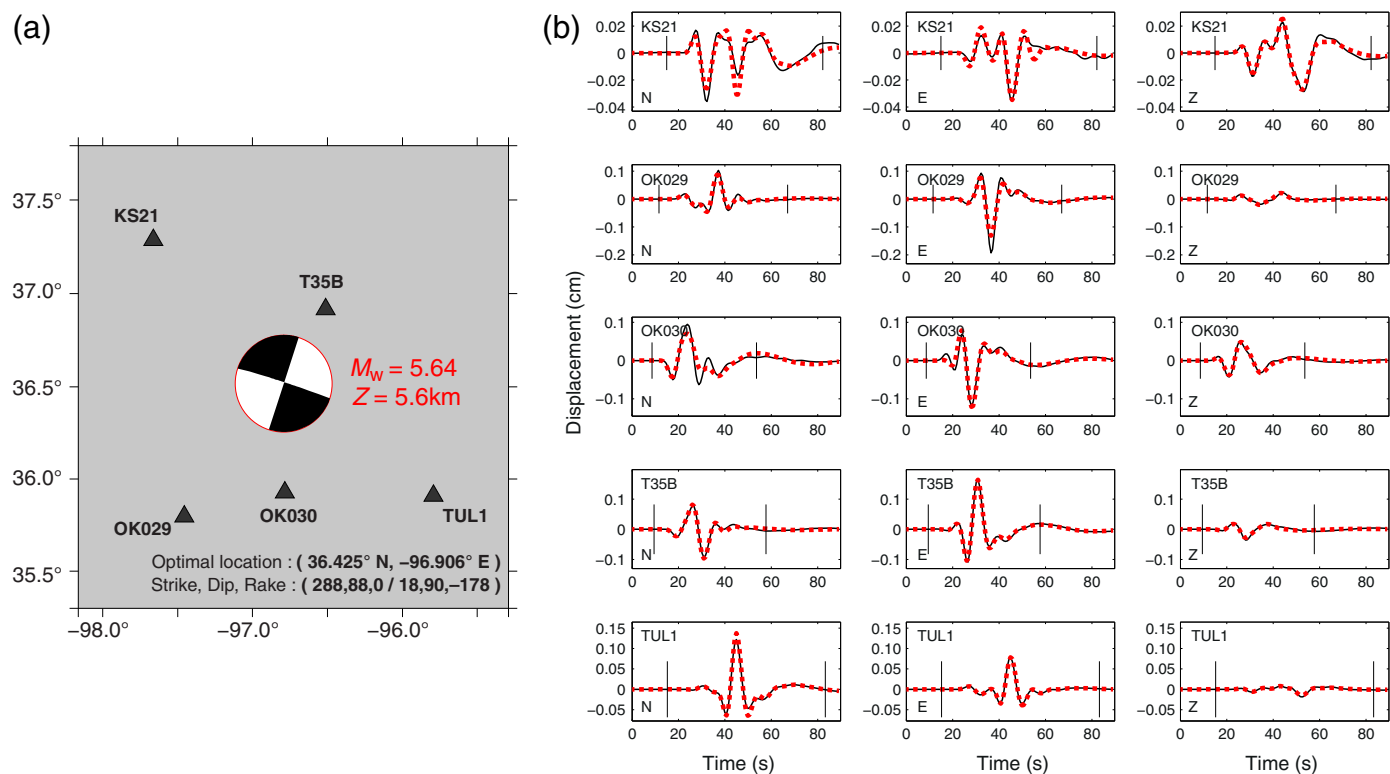
Finally, the time-series interferograms are geocoded and subsampled based on model resolution (Lohman and Simons, 2005), with a minimum spacing of 2 km between data points in the near field (i.e., approximately within 15 km of fault trace, see Fig. 4c).

We find that the earthquake is responsible for two areas of significant LoS motion, taking the form of two distinct lobes characteristic of a blind strike-slip fault (Fig. 4a). The location of the fringes, to the west of the epicenter, is consistent with this displacement being induced by a combination of east–west and vertical motion. Peak-to-peak amplitude of LoS displacement reaches 3 cm over a distance of 10 km. The shape and magnitude of this fringe pattern provide strong constraints on the location and depth of the rupture area. Other features visible in the coseismic interferogram (Figs. 3 and 4) likely reflect residual atmospheric artifacts with maximum amplitude of  $\sim 1.5$  cm.

## SEISMOLOGICAL DATA AND VELOCITY MODEL

The earthquake has been recorded by local broadband seismometers from GS, N4, TA, and OK networks. Even if some of the closest stations are clipped, the subset of five stations shown in Figure 5a offers a good azimuthal coverage of the earthquake. We first conduct a point-source inversion of these data to determine the first-order characteristics of the earthquake (focal mechanism, centroid depth) together with a suitable structure model. The method used, hereafter MECAVEL, simultaneously optimizes (with the Neighborhood Algorithm of Sambridge, 1999) the source parameters and a simplified velocity model, parameterized by a superficial low-velocity layer above a crustal increasing gradient. The searched source param-





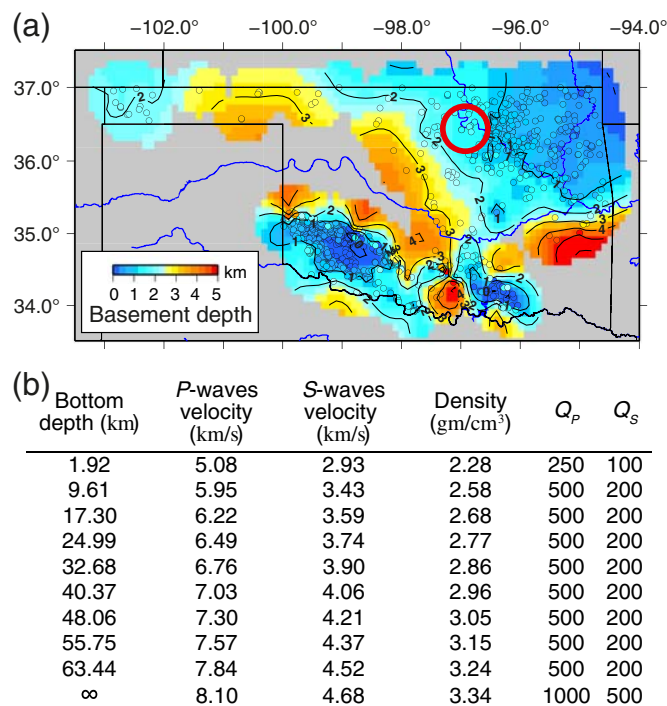
▲ **Figure 5.** Point-source inversion. (a) Local stations (triangles) and optimal source parameters from MECAVEL point-source inversion. Note that the moment magnitude is found to be slightly larger (5.71) in the finite-fault inversion. (b) Comparison between observed (thin continuous line) and modeled (thick dashed line) three-component (N, E, Z) seismograms for the point-source inversion. Here, data and synthetics are filtered between 0.02 and 0.125 Hz. The color version of this figure is available only in the electronic edition.

eters include the strike, dip, and rake of the focal mechanism, the centroid location, the source origin time and duration, and the moment magnitude. Waveform modeling in the 1D velocity model is performed with the discrete wavenumber method of Bouchon (1981). In the MECAVEL method, the three-component displacement waveforms are bandpassed between a low-frequency ( $F_{c1}$ ) and a high-frequency ( $F_{c2}$ ) threshold.  $F_{c1}$  is typically chosen above the low-frequency noise that may affect the waveforms of a moderate earthquake, and  $F_{c2}$  is mostly controlled by the limited ability of a 1D model for the waveform modeling.  $F_{c2}$  also has to be chosen below the earthquake corner frequency, as the earthquake time history is simply modeled by a triangular source time function. In the specific case of the Pawnee earthquake,  $F_{c1}$  is chosen at 0.02 Hz (classical value for a moderate earthquake) and  $F_{c2}$  at 0.125 Hz; the latter value can here be chosen higher than in more complex media (e.g., in subduction zones), which enlarges the frequency range and hence the parameter resolution. Another application of the MECAVEL method in a different context can be found in Mercier de Lépinay *et al.* (2011), where the aftershocks of the 2010 Haiti earthquake are analyzed.

We show the optimal source parameters determined by the MECAVEL method in Figure 5a and the associated waveform agreement in Figure 5b. We find that the focal mechanism of the Pawnee earthquake is consistent with nearly pure left-lateral strike slip on an ESE–WNW-trending vertical fault, in

agreement with the alignment of aftershocks reported by Yeck, Weingarten, *et al.* (2016; Fig. 1). The epicentral centroid location, shifted about 2 km in the east direction compared to the USGS epicenter, also favors the activation of the plane delineated by aftershocks. The centroid depth is constrained at 5.6 km, that is, well within the Precambrian basement. Figure 6b shows the optimized velocity model, whose scope is to represent an equivalent propagation medium, possibly not directly interpretable in terms of real structure. We, however, note that the inverted thickness of the shallow layer (about 2 km) agrees well with the information available for the basement depth in the epicentral area (Fig. 6a; Campbell and Weber, 2006).

More precise analyses of the Pawnee earthquake (see the Kinematic Slip Inversion section) are required to model the waveforms at higher frequency. To do so, we consider the local displacement waveforms in the frequency range [0.02–0.5 Hz] and restrain our analysis to the early part of the seismograms, comprised between the first *P*-wave arrival and a few seconds after the *S*-wave arrival (Fig. 7b). This excludes the high-frequency surface waves, which carry more information about unknown characteristics of the propagation medium than on the source. We also include body-wave records at teleseismic distances from the Federation of Digital Seismograph Networks (Incorporated Research Institutions for Seismology [IRIS]–USGS and GEOSCOPE networks), band-pass filtered in displacement between 0.0125 and 0.5 Hz. Three *P*-wave and



▲ **Figure 6.** (a) Depth to the basement in Oklahoma deduced from well data (Campbell and Weber, 2006). Area of Pawnee earthquake is indicated by the circle. Background is an interpolation of individual well data, indicated by dots. (b) Velocity model from MECAVEL point-source inversion. The color version of this figure is available only in the electronic edition.

seven *SH*-wave records with good SNR in this frequency range are selected (Fig. 7a).

## KINEMATIC SLIP INVERSION

The geodetic and seismic data are jointly inverted using the method of Delouis *et al.* (2002; see also Delouis *et al.*, 2010; Grandin *et al.*, 2015), adapted here for a moderate magnitude earthquake configuration. The modeled fault is subdivided into nine columns along strike and seven rows along dip, measuring 1.5 km along strike and dip. The geometry is held fixed according to parameters determined from the point-source inversion (strike 288°, dip 88°). Fault location is determined by fixing one grid node to the coordinates of the USGS epicenter (36.425° N, 96.929° W, depth 5.6 km). Subfaults forming the upper and lower edges of the modeled finite fault are centered on depths of 2.6 and 11.6 km, respectively.

The waveforms are modeled by summing point sources located at the center of each subfault, with individual source time functions consisting of two isosceles triangular shaped functions with duration 1 s. The onset time of slip together with the rake angle and slip amount of individual point source are determined by a simulated annealing optimization algorithm. The onset time of slip is constrained by average rupture velocities allowed to vary between 0.5 and 3 km/s, and the rake angle is constrained to remain at  $\pm 15^\circ$  from the pure strike-slip

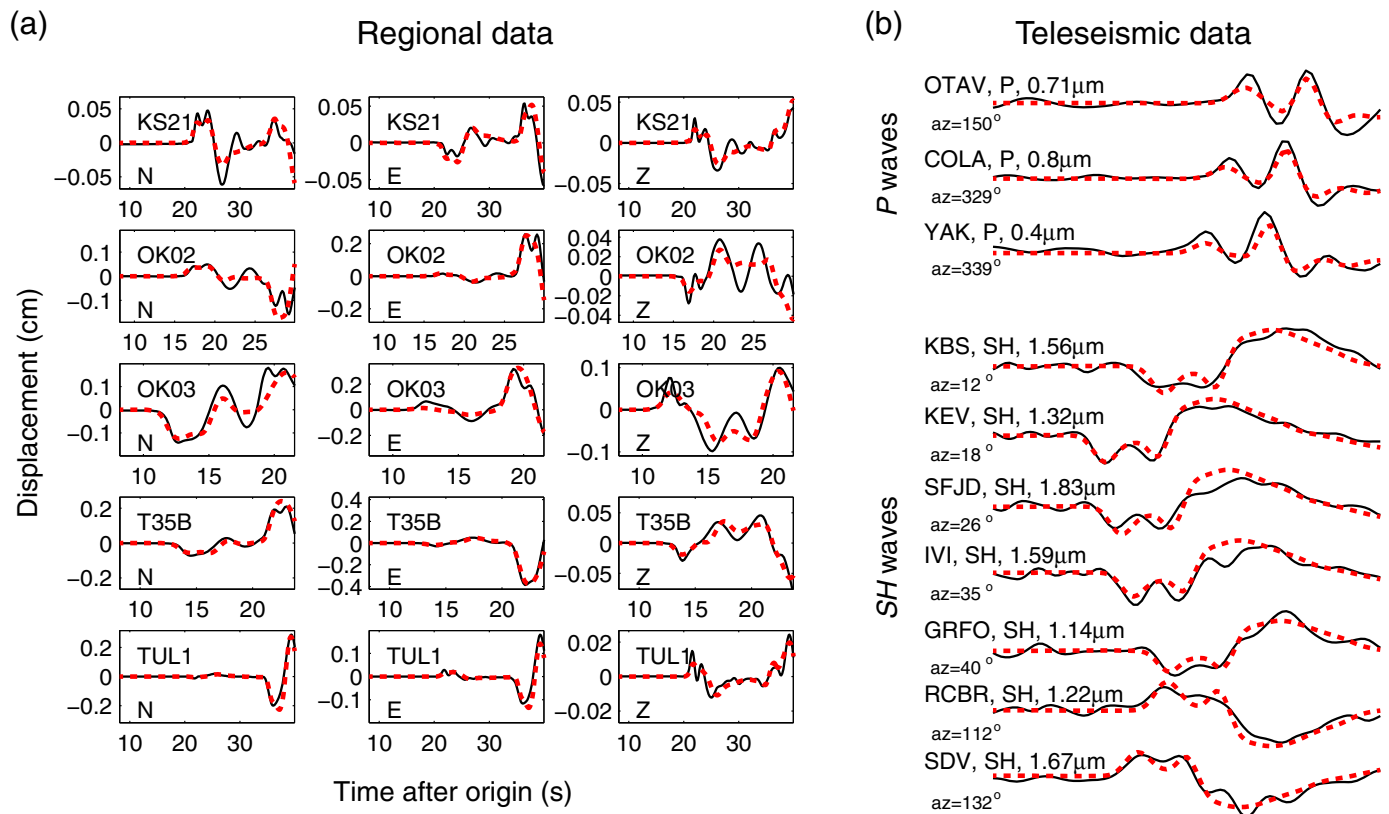
mechanism determined in the MECAVEL inversion. The cost function to be minimized includes the average of the rms misfit of each data set (InSAR, regional data, and teleseismic data) as well as the spatial and temporal roughness of coseismic slip, rupture velocities, and rake angle variations. All synthetics are computed in the velocity model optimized in the Seismological Data and Velocity Model section through the MECAVEL point-source approach (Fig. 6b). Specifically, local synthetic seismograms and teleseismic *P* and *SH* displacements are computed using the discrete wavenumber method of Bouchon (1981) and the reciprocity approach of Bouchon (1976), respectively. Static displacements for InSAR are computed using the static Green's function approach of Wang *et al.* (2003).

The space–time evolution of slip determined by the joint inversion of InSAR, local, and teleseismic seismological data is shown in Figures 8 and 9. The seismic moment of  $M_0 = 4.64 \times 10^{17}$  N·m ( $M_w$  5.71), slightly larger than in the MECAVEL point-source inversion, is released in 4 s (Fig. 8). We find slip to be concentrated in an 8-km-long rupture area, at depths comprised between 4 and 9 km, over which the slip reaches at least 40 cm (Fig. 9). The aftershocks of the Pawnee earthquake appear to delineate the upper edge of the main slip area (Fig. 9). Significant slip ( $> 10$  cm) at shallow depth is excluded thanks to the high model resolution in the 0–4-km depth range provided by the InSAR data. After a slow start in the hypocentral area during the first second, the rupture propagates both eastward (in agreement with the location of the MECAVEL centroid) and downward (Fig. 8). The rupture therefore remains entirely confined within the basement, failing to enter the superficial sedimentary cover. These first-order features remain valid when using the hypocenter depth of 4.7 km reported by Yeck, Hayes, *et al.* (2016), albeit at the cost of a slightly degraded fit and increased space–time complexity of the source.

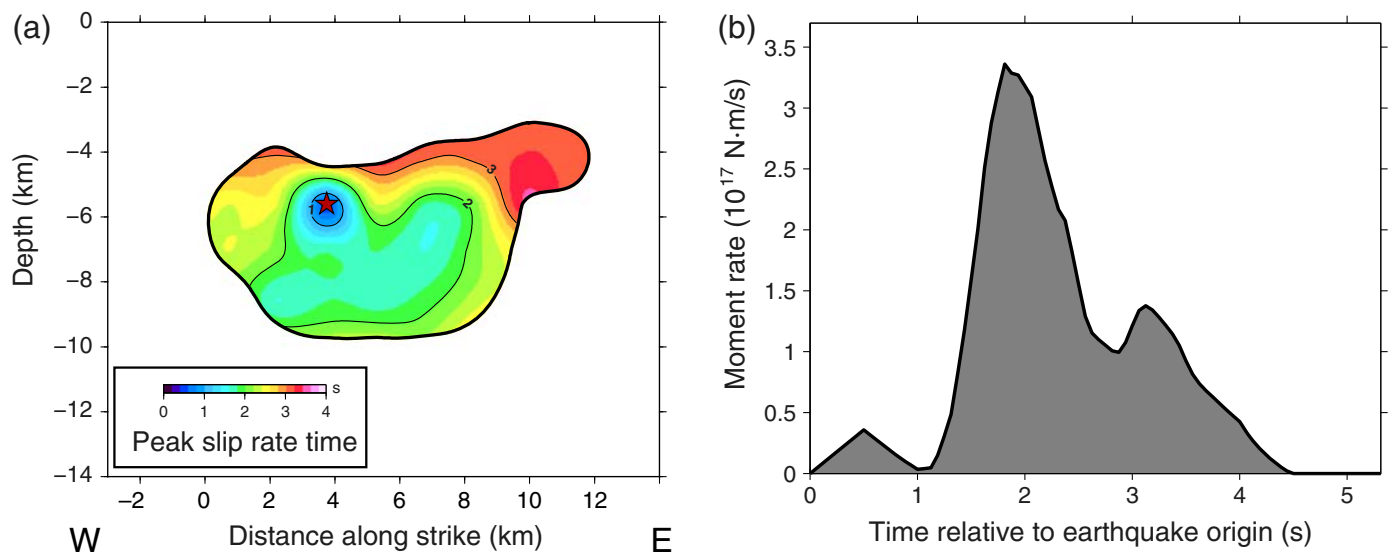
## DISCUSSION AND CONCLUSIONS

Although it is generally difficult to ascertain the causal relationship between wastewater injection and the occurrence of a particular earthquake, the context strongly suggests that the 2016 Pawnee earthquake represents another case of induced seismicity (Fig. 10). Indeed, in the year preceding the mainshock, at least two wells were injecting saltwater at rates exceeding 500 m<sup>3</sup>/day within 7 km of the epicenter (wells OLDHAM and SCROGGINS) (Fig. 10a,b). Furthermore, an increase of the injection rate was reported at two wells located near the epicenter of the Pawnee earthquake. At well SCROGGINS (7 km), the injection rate was increased by more than 50% in the three months prior to the earthquake, reaching a peak of 1100 m<sup>3</sup>/day in early August 2016 (Fig. 10c). It may be argued that these changes could have destabilized the fault involved in the Pawnee sequence, since changes in injection rates with the same order of magnitude and taking place over similar distance and duration were reported before the nearby Cushing and Milan seismic sequences (McNamara, Hayes, *et al.*, 2015; Choy *et al.*, 2016).

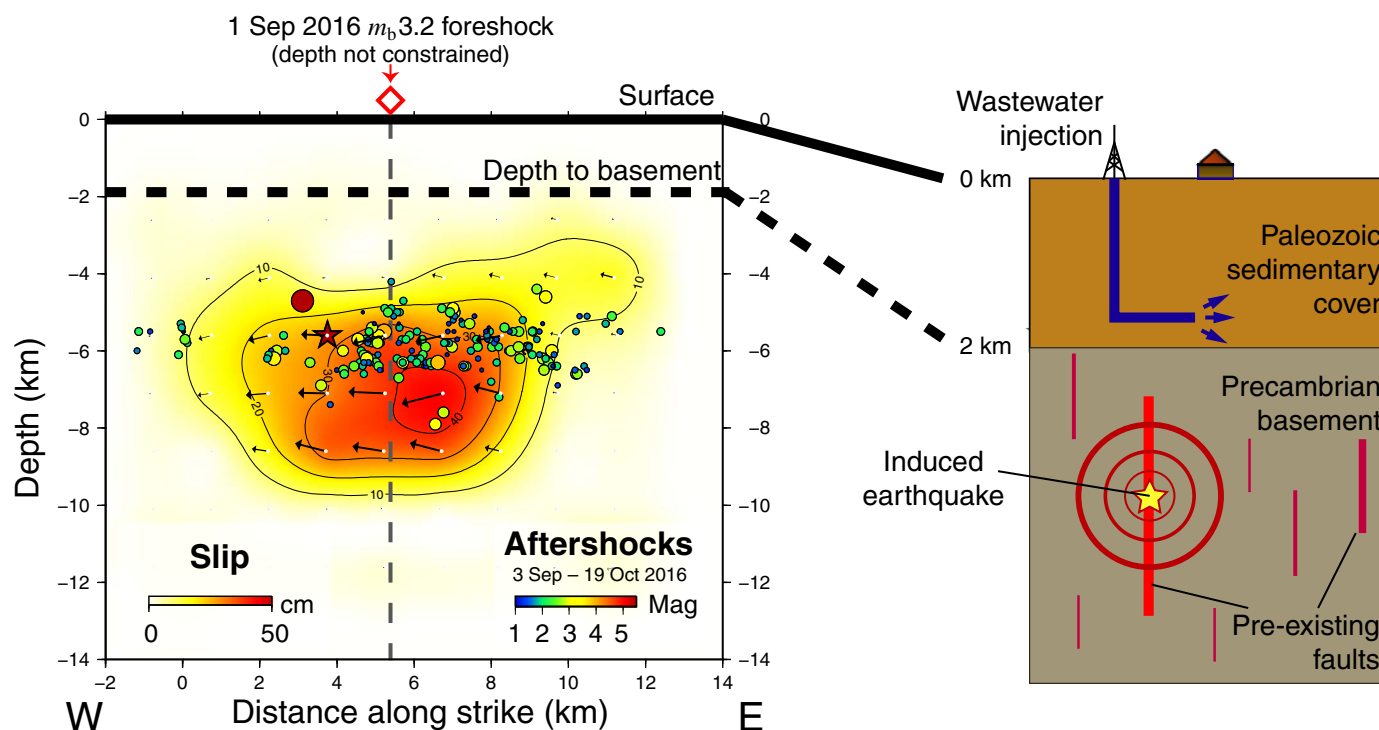
On a shorter time scale, even more rapid changes in injection rate can be noticed. At well NORMAN (8 km), in spite



▲ **Figure 7.** Finite-source kinematic inversion. (a) Observed (thin continuous line) and modeled (thick dashed line) waveforms at local stations. Three-component (N, E, Z) displacement seismograms (filtered between 0.02 and 0.5 Hz) are shown and modeled in a window starting from the *P*-wave arrival and stopping a few seconds after the *S*-wave arrival. (b) Observed (thin continuous line) and modeled (thick dashed line) waveforms at teleseismic distances. *P* waves are shown in the three subplots at the top, and *SH* waves on next seven subplots below, both being band-pass filtered in displacement between 0.0125 and 0.5 Hz. Duration shown is 21 and 30 s for *P* and *SH* waves, respectively. Name, azimuth of the station (*az*), and maximum amplitude in microns are indicated for each seismogram. The color version of this figure is available only in the electronic edition.



▲ **Figure 8.** (a) Time of peak slip-rate release referenced to the hypocentral time for the area of significant slip. Star marks the hypocenter location. (b) Source time function derived from the kinematic slip inversion. The color version of this figure is available only in the electronic edition.



▲ **Figure 9.** Slip model of the Pawnee earthquake from joint kinematic inversion of geodetic and seismological data. Aftershocks are from Yeck, Hayes, *et al.* (2016). Diamond and vertical dashed line indicate 1 September 2016 foreshock (Yeck, Hayes, *et al.*, 2016). Basement depth is indicated by the horizontal dashed line. Star marks the hypocenter location. The color version of this figure is available only in the electronic edition.

of a significantly lower average injection rate of only 35 m<sup>3</sup>/day in the two months preceding the Pawnee earthquake, the injection rate was abruptly increased by a factor of 6 on 28 August 2016, that is, five days before the mainshock (see inset in Fig. 10). According to Yeck, Hayes, *et al.* (2016), an  $m_b$  3.2 foreshock was recorded in the epicentral area of the Pawnee earthquake on 1 September 2016 (diamond in Figs. 1, 9, and 10). Retrospective analysis of microseismicity in the epicentral area of the Pawnee earthquake revealed that this foreshock belonged to an episode of enhanced seismicity that had started 90 days before the mainshock (Walter *et al.*, 2017). Should the hypothesis of an injection-induced earthquake hold for the 3 September Pawnee mainshock, then these foreshocks may represent a case of precursory seismic activity. However, in spite of the spatial and temporal coincidence between seismic activity and changes in injection rates in the Pawnee area, categorizing with certainty the Pawnee earthquake as an induced earthquake would require further investigation, in particular the careful validation of reports made by disposal well operators.

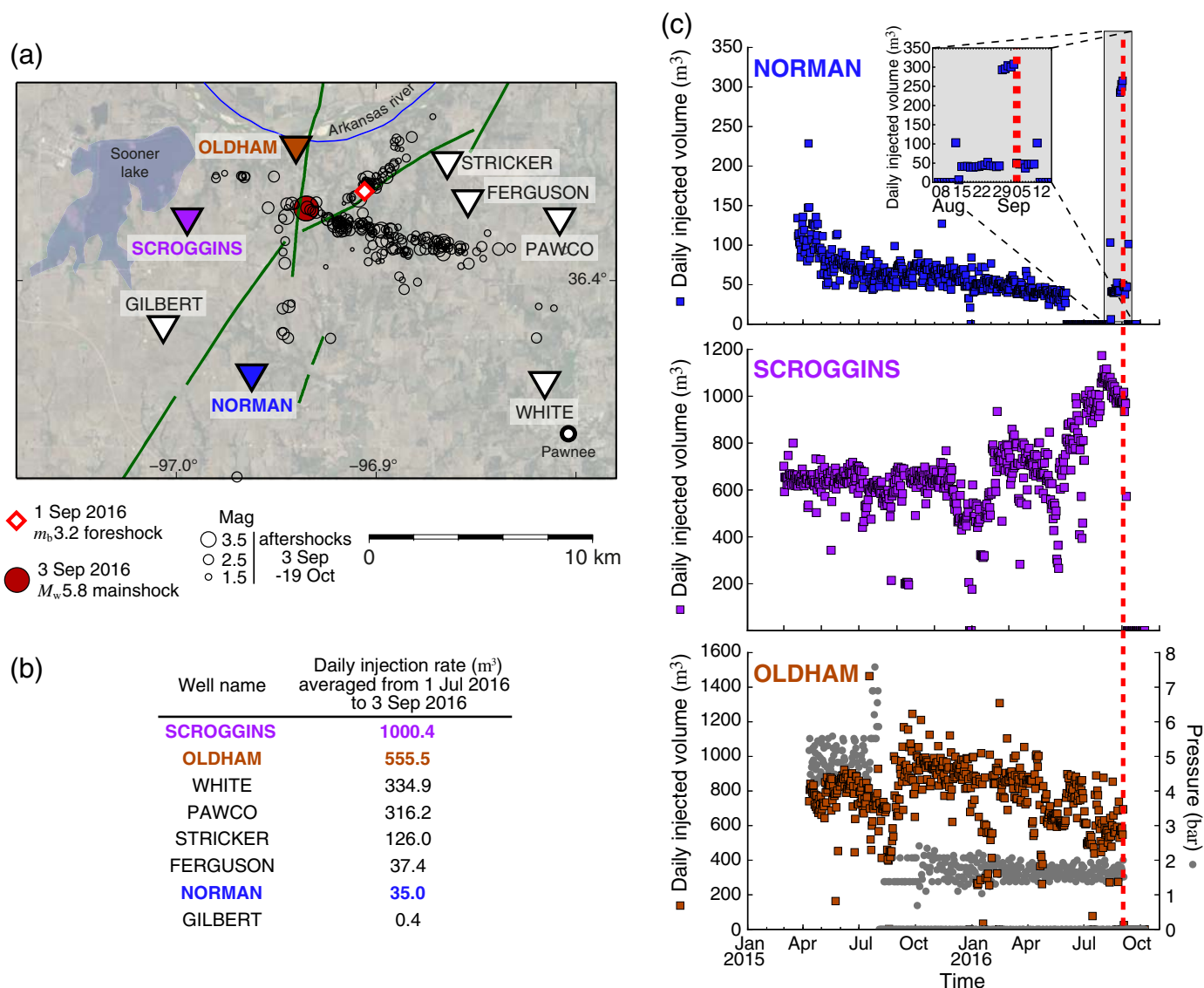
Our study reveals that nucleation of the 2016 Pawnee earthquake occurred deep into the basement, whose top lies at 2 km under the surface (Fig. 6a). The earthquake may therefore result from destabilization of a fault buried 3–4 km below the depth range where fluids are being injected. Similarly deep aftershocks were reported following the 2011 M 5.7 Prague (McNamara, Benz, *et al.*, 2015) and M 5.1 2014 Fairview (Yeck, Weingarten, *et al.*, 2016) earthquakes. Two physical mechanisms can explain this induced response: (a) pore pressure increase on

the fault plane, and (b) remote stress triggering due to host rock poroelastic deformation (Ellsworth, 2013). Although the latter mechanism decays rapidly over short ranges, the former is more problematic to quantify. Indeed, the presence of pervasive fracturing within the basement makes it possible for fluid-pressure changes to be conveyed down to great depth (McGarr, 2014). This effect heavily distorts the shape of the perturbed volume of surrounding rocks away from the spherical shape predicted by a simple isotropic theoretical model (Chang and Segall, 2016). The resulting magnitude and location of fluid-pressure perturbations are therefore subject to large uncertainties.

Whichever mechanism should apply, the link between the 2016 Pawnee earthquake and shallow injection activities is not straightforward. The rupture has nucleated well into the basement, and coseismic slip seems to have died down as it propagated up-dip (Fig. 8). The rupture therefore failed to enter the superficial sedimentary layers that cover the basement, even though the effect of fluid injection would be expected to be highest at the shallow depths where injection is taking place. Instead, the Pawnee rupture activated a previously unmapped fault entirely confined into the basement, thereby illustrating how dormant structures can sometimes be only recognized *a posteriori*.

Nevertheless, the orientation of the fault involved during the 2016 Pawnee mainshock is not random. Akin to other recent earthquakes in Oklahoma, the focal mechanism of the Pawnee earthquake is also consistent with the activation of strike-slip faults striking either northeast–southwest (right lateral) or east–southeast–west–northwest (left lateral) (McNamara,





▲ **Figure 10.** (a) Location of main wastewater injection wells (inverted triangles) operating in the Pawnee area prior to the 3 September 2016  $M_w$  5.8 Pawnee earthquake. Open circles are aftershocks from Yeck, Hayes, et al. (2016). Diamond indicates the 1 September 2016 foreshock (Yeck, Hayes, et al., 2016). (b) Daily injection rate averaged from 1 July to 3 September 2016 for wells indicated in (a). (c) Evolution of daily injection rates (squares) for three selected wells from 1 January 2015 to 1 November 2016. Circles show pressure data, when available. Date of Pawnee mainshock is indicated by the vertical dashed line. (Inset) A blowup of injection history for well NORMAN near the date of the Pawnee earthquake (gray area in c). The color version of this figure is available only in the electronic edition.

Benz, et al., 2015). This consistency highlights the brittle response to a coherent background regional stress, with maximum compressive stress oriented  $\sim$ east–west, suggesting that such well-oriented faults should be considered in priority in future seismic-hazard assessment models (Walsh and Zoback, 2016).

More strikingly though, these recent earthquakes are also kinematically consistent with surface displacement on the Meers fault in southwest Oklahoma, the only fault where a Holocene surface rupture is clearly documented in the area (Crone and Luza, 1990; Fig. 1). This key observation suggests that, despite a lack of measurable present-day tectonic strain in Oklahoma, this intraplate region may be seismically active in the long term. Such a behavior has been identified in several

stable continental regions, including central United States, where rare, energetic earthquakes have been reported in the historical past or inferred from paleoseismology (Calais et al., 2016; Liu and Stein, 2016). Hence, in Oklahoma, fluid injection might stimulate the occurrence of earthquakes that would otherwise occur infrequently. In other words, wastewater injection activities may force the natural process to be played in fast forward. Although the recent enforcement of a regulation putting a cap on saltwater injection rates appears to have led to a significant decrease in the seismicity rate since the first quarter of 2016 (Langenbruch and Zoback, 2016; Yeck, Hayes, et al., 2016), the actual improvement gained in terms of seismic hazard is still unclear. Unless actions to mitigate or stop those activities

are taken, the implacable projection of the Gutenberg–Richter law from current seismicity trends (van der Elst *et al.*, 2016) makes it likely that at least a few more earthquakes with magnitudes exceeding  $M$  5.5, and possibly higher, will strike Oklahoma in the next years to decades.

In conclusion, the Pawnee earthquake occurred in the crystalline basement, not in the sedimentary cover. The earthquake generated detectable surface deformation which, in addition to dynamic shaking, could affect infrastructure in these regions (roads, pipelines, settling ponds, etc.). Spaceborne InSAR observations of significant earthquakes, in combination with regional and teleseismic seismological data, while not necessarily directly informing triggering mechanisms, provide an important additional input for pore pressure and hazard modeling studies.

## DATA AND RESOURCES

We downloaded Sentinel-1 data processed to level-1 (SLC) format from the Plateforme d'Exploitation des Produits Sentinel (PEPS) website (<https://peps.cnes.fr/rocket/>, last accessed March 2017). We downloaded the restituted orbits and, when available, precise orbits, from European Space Agency's (ESA's) Sentinel-1 website (<https://qc.sentinel1.eo.esa.int/>, last accessed March 2017). We used 10-m resolution digital elevation model from the National Elevation Dataset (NED), made available by U.S. Geological Survey (USGS; <http://earthexplorer.usgs.gov/>, last accessed March 2017). Teleseismic data are from the Federation of Digital Seismograph Networks (FDSNs). Local and regional data are from GS, N4, TA, and OK networks, made available through Incorporated Research Institutions for Seismology (IRIS). A statewide wastewater disposal well database is available from the Oklahoma Corporation Commission (OCC) website (<http://www.occeweb.com/og/ogdatafiles2.htm>, last accessed January 2017). We used daily reported volumes of all Arbuckle disposal wells, submitted by operators via the OCC file system ([ftp://ftp.occeweb.com/OG\\_DATA/Dly1012d.ZIP](ftp://ftp.occeweb.com/OG_DATA/Dly1012d.ZIP), last accessed January 2017). The data for the 3 September 2016 Pawnee earthquake can be found at <https://earthquake.usgs.gov/earthquakes/eventpage/us10006jxs#dyfi> (last accessed March 2017). ☒

## ACKNOWLEDGMENTS

We are grateful to the Incorporated Research Institutions for Seismology–U.S. Geological Survey (IRIS-USGS) and GEOSCOPE networks (belonging to the Federation of Digital Seismograph Networks), and to the GS, N4, TA, and OK networks, for public access to the data used in the teleseismic and regional seismological analyses, respectively. We thank two anonymous reviewers and Editor Xiaowei Chen for providing constructive comments on the article. This project was supported by Programme National de Télédétection Spatiale Grant “PNTS-2015-09.” This is Institut de Physique du Globe de Paris (IPGP) Contribution Number 3825.

## REFERENCES

- Barnhart, W. D., H. M. Benz, G. P. Hayes, J. L. Rubinstein, and E. Bergman (2011). Seismological and geodetic constraints on the 2011  $M_w$  5.3 Trinidad, Colorado earthquake and induced deformation in the Raton basin, *J. Geophys. Res.* **119**, no. 10, doi: [10.1002/2014JB011227](https://doi.org/10.1002/2014JB011227).
- Benz, H. M., N. D. McMahon, R. C. Aster, D. E. McNamara, and D. B. Harris (2015). Hundreds of earthquakes per day: The 2014 Guthrie, Oklahoma, earthquake sequence, *Seismol. Res. Lett.* **86**, no. 5, 1318–1325.
- Berardino, P., G. Fornaro, R. Lanari, and E. Sansosti (2002). A new algorithm for surface deformation monitoring based on small baseline differential SAR interferograms, *IEEE Trans. Geosci. Remote Sens.* **40**, no. 11, 2375–2383.
- Bouchon, M. (1976). Teleseismic body wave radiation from a seismic source in a layered medium, *Geophys. J. Int.* **47**, no. 3, 515–530.
- Bouchon, M. (1981). A simple method to calculate Green's functions for elastic layered media, *Bull. Seismol. Soc. Am.* **71**, no. 4, 959–971.
- Calais, E., T. Camelbeeck, S. Stein, M. Liu, and T. Craig (2016). A new paradigm for large earthquakes in stable continental plate interiors, *Geophys. Res. Lett.* **43**, no. 20, doi: [10.1002/2016GL070815](https://doi.org/10.1002/2016GL070815).
- Campbell, J. A., and J. A. Weber (2006). Wells drilled to basement in Oklahoma, *Oklahoma Geological Survey Special Publication 2006–1*.
- Cavalié, O., M. P. Doin, C. Lasserre, and P. Briole (2007). Ground motion measurement in the Lake Mead area, Nevada, by differential synthetic aperture radar interferometry time series analysis: Probing the lithosphere rheological structure, *J. Geophys. Res.* **112**, no. B3, doi: [10.1029/2006JB004344](https://doi.org/10.1029/2006JB004344).
- Chang, K. W., and P. Segall (2016). Injection-induced seismicity on basement faults including poroelastic stressing, *J. Geophys. Res.* **121**, doi: [10.1002/2015JB012561](https://doi.org/10.1002/2015JB012561).
- Choy, G. L., J. L. Rubinstein, W. L. Yeck, D. E. McNamara, C. S. Mueller, and O. S. Boyd (2016). A rare moderate-sized ( $M_w$  4.9) earthquake in Kansas: Rupture process of the Milan, Kansas, earthquake of 12 November 2014 and its relationship to fluid injection, *Seismol. Res. Lett.* **87**, no. 6, 1433–1441.
- Crone, A. J., and K. V. Luza (1990). Style and timing of Holocene surface faulting on the Meers fault, southwestern Oklahoma, *Geol. Soc. Am. Bull.* **102**, no. 1, 1–17.
- Delouis, B., D. Giardini, P. Lundgren, and J. Salichon (2002). Joint inversion of InSAR, GPS, teleseismic, and strong-motion data for the spatial and temporal distribution of earthquake slip: Application to the 1999 Izmit mainshock, *Bull. Seismol. Soc. Am.* **92**, no. 1, 278–299.
- Delouis, B., J.-M. Nocquet, and M. Vallée (2010). Slip distribution of the February 27, 2010  $M_w$  = 8.8 Maule earthquake, central Chile, from static and high-rate GPS, InSAR, and broadband teleseismic data, *Geophys. Res. Lett.* **37**, no. 17, doi: [10.1029/2010GL043899](https://doi.org/10.1029/2010GL043899).
- Doin, M. P., C. Lasserre, G. Peltzer, O. Cavalié, and C. Doubre (2009). Corrections of stratified tropospheric delays in SAR interferometry: Validation with global atmospheric models, *J. Appl. Geophys.* **69**, no. 1, 35–50.
- Doin, M.-P., S. Guillaso, R. Jolivet, C. Lasserre, F. Lodge, G. Ducret, and R. Grandin (2011). Presentation of the small baseline NSBAS processing chain on a case example: The ETNA deformation monitoring from 2003 to 2010 using Envisat data, *Proc. of the Fringe Symposium, European Space Agency*, 3434–3437.
- Ellsworth, W. L. (2013). Injection-induced earthquakes, *Science* **341**, no. 6142, doi: [10.1126/science.1225942](https://doi.org/10.1126/science.1225942).
- Frohlich, C., H. DeShon, B. Stump, C. Hayward, M. Hornbach, and J. I. Walter (2016). A historical review of induced earthquakes in Texas, *Seismol. Res. Lett.* **87**, no. 6, doi: [10.1785/0220160016](https://doi.org/10.1785/0220160016).
- Gesch, D., M. Oimoen, S. Greenlee, C. Nelson, M. Steuck, and D. Tyler (2002). The national elevation dataset, *Photogramm. Eng. Remote Sens.* **68**, no. 1, 5–32.
- Geudtner, D., R. Torres, P. Snoei, M. Davidson, and B. Rommen (2014). Sentinel-1 system capabilities and applications, *Geoscience and Re-*

- mote Sensing Symposium (IGARSS), 2014 IEEE International, IEEE*, 1457–1460.
- Goldstein, R. M., and C. L. Werner (1998). Radar interferogram filtering for geophysical applications, *Geophys. Res. Lett.* **25**, no. 21, 4035–4038.
- Goldstein, R. M., H. A. Zebker, and C. L. Werner (1988). Satellite radar interferometry: Two-dimensional phase unwrapping, *Radio Sci.* **23**, no. 4, 713–720.
- González, P. J., K. F. Tiampo, M. Palano, F. Cannavó, and J. Fernández (2012). The 2011 Lorca earthquake slip distribution controlled by groundwater crustal unloading, *Nat. Geosci.* **5**, no. 11, 821–825, doi: [10.1038/ngeo1610](https://doi.org/10.1038/ngeo1610).
- Grandin, R. (2015). Interferometric processing of SLC Sentinel-1 TOPS data, *Proc. of the 2015 ESA Fringe Workshop*, ESA Special Publication, Vol. 731.
- Grandin, R., M. Vallée, C. Satriano, R. Lacassin, Y. Klinger, M. Simoes, and L. Bollinger (2015). Rupture process of the  $M_w = 7.9$  2015 Gorkha earthquake (Nepal): Insights into Himalayan megathrust segmentation, *Geophys. Res. Lett.* **42**, no. 20, 8373–8382.
- Holland, A. A. (2015). Preliminary fault map of Oklahoma, *Oklahoma Geol. Surv. Open-File Rept. OF5-2015*.
- Hough, S. E., and M. Page (2015). A century of induced earthquakes in Oklahoma? *Bull. Seismol. Soc. Am.* **105**, no. 6, 2863–2870.
- Keranen, K. M., H. M. Savage, G. A. Abers, and E. S. Cochran (2013). Potentially induced earthquakes in Oklahoma, USA: Links between wastewater injection and the 2011  $M_w$  5.7 earthquake sequence, *Geology* **41**, no. 6, 699–702.
- Keranen, K. M., M. Weingarten, G. A. Abers, B. A. Bekins, and S. Ge (2014). Sharp increase in central Oklahoma seismicity since 2008 induced by massive wastewater injection, *Science* **345**, no. 6195, 448–451.
- Langenbruch, C., and M. D. Zoback (2016). How will induced seismicity in Oklahoma respond to decreased saltwater injection rates? *Sci. Adv.* **2**, no. 11, e1601542, doi: [10.1126/sciadv.1601542](https://doi.org/10.1126/sciadv.1601542).
- Liu, M., and S. Stein (2016). Mid-continental earthquakes: Spatiotemporal occurrences, causes, and hazards, *Earth Sci. Rev.* **162**, 364–386.
- Lohman, R. B., and M. Simons (2005). Some thoughts on the use of InSAR data to constrain models of surface deformation: Noise structure and data downsampling, *Geochem. Geophys. Geosys.* **6**, no. 1, doi: [10.1029/2004GC000841](https://doi.org/10.1029/2004GC000841).
- López-Quiroz, P., M.-P. Doin, F. Tupin, P. Briole, and J.-M. Nicolas (2009). Time series analysis of Mexico City subsidence constrained by radar interferometry, *J. Appl. Geophys.* **69**, no. 1, 1–15.
- Matson, S. (2013). Mississippi lime play: From outcrop to subsurface—The evolution of a play, *AAPG Search and Discovery Article 110170*.
- McGarr, A. (2014). Maximum magnitude earthquakes induced by fluid injection, *J. Geophys. Res.* **119**, no. 2, 1008–1019.
- McNamara, D. E., H. M. Benz, R. B. Herrmann, E. A. Bergman, P. Earle, A. Holland, R. Baldwin, and A. Gassner (2015). Earthquake hypocenters and focal mechanisms in central Oklahoma reveal a complex system of reactivated subsurface strike-slip faulting, *Geophys. Res. Lett.* **42**, no. 8, 2742–2749.
- McNamara, D. E., G. Hayes, H. M. Benz, R. Williams, N. D. McMahon, R. Aster, A. Holland, T. Sickbert, R. Herrmann, R. Briggs, et al. (2015). Reactivated faulting near Cushing, Oklahoma: Increased potential for a triggered earthquake in an area of United States strategic infrastructure, *Geophys. Res. Lett.* **42**, no. 20, 8328–8332.
- Mercier de Lépinay, B., A. Deschamps, F. Klingelhoefer, Y. Mazabraud, B. Delouis, V. Clouard, Y. M. Hello, J. Crozon, B. Marcaillou, D. Graindorge, et al. (2011). The 2010 Haiti earthquake: A complex fault pattern constrained by seismologic and tectonic observations, *Geophys. Res. Lett.* **38**, L22305, doi: [10.1029/2011GL049799](https://doi.org/10.1029/2011GL049799).
- Murray, K. E. (2014). Class II underground injection control well data for 2010–2013 by geologic zones of completion, Oklahoma, *Oklahoma Geol. Surv. Open-File Rept. OF1-2014*.
- Murray, K. E. (2015). Class II saltwater disposal for 2009–2014 at the annual-, state-, and county-scales by geologic zones of completion, Oklahoma, *Oklahoma Geol. Surv. Open-File Rept. OF5-2015*, doi: [10.13140/RG.2.1.4841.7364](https://doi.org/10.13140/RG.2.1.4841.7364).
- Rosen, P. A., S. Hensley, G. Peltzer, and M. Simons (2004). Updated repeat orbit interferometry package released, *Eos Trans. AGU* **85**, no. 5, 47.
- Rubinstein, J. L., and A. B. Mahani (2015). Myths and facts on wastewater injection, hydraulic fracturing, enhanced oil recovery, and induced seismicity, *Seismol. Res. Lett.* **86**, no. 4, 1060–1067.
- Sambridge, M. (1999). Geophysical inversion with a neighbourhood algorithm—I. Searching a parameter space, *Geophys. J. Int.* **138**, 479–494, doi: [10.1046/j.1365-246X.1999.00876.x](https://doi.org/10.1046/j.1365-246X.1999.00876.x).
- Schmidt, D. A., and R. Bürgmann (2003). Time-dependent land uplift and subsidence in the Santa Clara valley, California, from a large interferometric synthetic aperture radar data set, *J. Geophys. Res.* **108**, no. B9, doi: [10.1029/2002JB002267](https://doi.org/10.1029/2002JB002267).
- Shirzaei, M., W. L. Ellsworth, K. F. Tiampo, P. J. Gonzalez, and M. Manga (2016). Surface uplift and time-dependent seismic hazard due to fluid injection in eastern Texas, *Science* **353**, no. 6306, 1416–1419.
- van der Elst, N. J., M. T. Page, D. A. Weiser, T. H. W. Goebel, and S. M. Hosseini (2016). Induced earthquake magnitudes are as large as (statistically) expected, *J. Geophys. Res.* **121**, 4575–4590, doi: [10.1002/2016JB012818](https://doi.org/10.1002/2016JB012818).
- Walsh, F. R., and M. D. Zoback (2015). Oklahoma's recent earthquakes and saltwater disposal, *Sci. Adv.* **1**, no. 5, e1500195, doi: [10.1126/sciadv.1500195](https://doi.org/10.1126/sciadv.1500195).
- Walsh, F. R., and M. D. Zoback (2016). Probabilistic assessment of potential fault slip related to injection-induced earthquakes: Application to north-central Oklahoma, USA, *Geology* **44**, no. 12, G38275.1.
- Walter, J., J. Chang, and P. J. Dotray (2017). Foreshock seismicity suggests gradual stress increase in the months prior to the 3 September 2016  $M_w$  5.8 Pawnee earthquake, *Seismol. Res. Lett.* **88**, no. 4, doi: [10.1785/0220170007](https://doi.org/10.1785/0220170007).
- Wang, R., F. L. Martín, and F. Roth (2003). Computation of deformation induced by earthquakes in a multi-layered elastic crust—FORTRAN programs EDGRN/EDCMP, *Comput. Geosci.* **29**, no. 2, 195–207.
- Weingarten, M., S. Ge, J. W. Godt, B. A. Bekins, and J. L. Rubinstein (2015). High-rate injection is associated with the increase in US mid-continent seismicity, *Science* **348**, no. 6241, 1336–1340.
- Yeck, W., M. Weingarten, H. Benz, D. McNamara, E. Bergman, R. Herrmann, J. Rubinstein, and P. Earle (2016). Far-field pressurization likely caused one of the largest injection induced earthquakes by reactivating a large preexisting basement fault structure, *Geophys. Res. Lett.* **43**, no. 19, doi: [10.1002/2016GL070861](https://doi.org/10.1002/2016GL070861).
- Yeck, W. L., G. P. Hayes, D. E. McNamara, J. L. Rubinstein, W. D. Barnhart, P. S. Earle, and H. M. Benz (2016). Oklahoma experiences largest earthquake during ongoing regional wastewater injection hazard mitigation efforts, *Geophys. Res. Lett.* **44**, doi: [10.1002/2016GL071685](https://doi.org/10.1002/2016GL071685).

Raphaël Grandin  
 Martin Vallée  
 Robin Lacassin  
 Institut de Physique du Globe de Paris  
 Sorbonne Paris Cité  
 Université Paris Diderot  
 UMR 7154 CNRS  
 1 rue Jussieu  
 75238 Paris, CEDEX 05  
 France  
[grandin@ipggp.fr](mailto:grandin@ipggp.fr)  
[vallee@ipggp.fr](mailto:vallee@ipggp.fr)  
[lacassin@ipggp.fr](mailto:lacassin@ipggp.fr)

Published Online 3 May 2017